processes

MDPI

Article

Impact-Rubbing Dynamic Behavior of Magnetic-Liquid Double Suspension Bearing under Different Protective Bearing Forms

Jianhua Zhao [1,2], Lanchun Xing [1], Sheng Li [1], Weidong Yan [1], Dianrong Gao [1] and Guojun Du [2,*]

[1] Fluid Power Transmission and Control Laboratory, Yanshan University, Qinhuangdao 066004, China; zhaojianhua@ysu.edu.cn (J.Z.); xinglanchun@foxmail.com (L.X.); 13394466235@163.com (S.L.); yanweidongysu@163.com (W.Y.); gaodr@ysu.edu.cn (D.G.)

[2] College of Civil Engineering and Mechanics, Yanshan University, Qinhuangdao 066004, China

* Correspondence: dugj2002@ysu.edu.cn

Abstract: The magnetic-liquid double suspension bearing (MLDSB) is a new type of suspension bearing, with electromagnetic suspension as the main part and hydrostatic supports as the auxiliary part. It can greatly improve the bearing capacity and stiffness of rotor-bearing systems and is suitable for a medium speed, heavy load, and frequent starting occasions. Compared with the active electromagnetic bearing system, the traditional protective bearing device is replaced by the hydrostatic system in MLDSB, and the impact-rubbing phenomenon can be restrained and buffered. Thus, the probability and degree of friction and wear between the rotor and the magnetic pole are reduced drastically when the electromagnetic system fails. In order to explore the difference in the dynamic behavior law of the impact-rubbing phenomenon between the traditional protection device and hydrostatic system, the dynamic equations of the rotor impact-rubbing in three kinds of protection devices (fixed ring/deep groove ball bearing/hydrostatic system) under electromagnetic failure mode are established, and the axial trajectory and motion law of the rotor are numerically simulated. Finally, the dynamic behavior characteristics of the rotor are compared and analyzed. The results show that: Among the three kinds of protection devices (fixed ring/deep groove ball bearing/hydrostatic system), the hydrostatic system has the least influence on bouncing time, impact-rubbing force, and impact-rubbing degree, and the maximum impact-rubbing force of MLDSB is greatly reduced. Therefore, the protective bear is not required to be installed in the MLDSB. This study provides the basis for the theory of the "gap impact-rubbing" of MLDSB under electromagnetic failure, and helps to identify electromagnetic faults.

Keywords: magnetic-liquid double suspension bearing; protecting bearing; hydrostatic system; impact-rubbing dynamics; electromagnetic failure

check for updates

Citation: Zhao, J.; Xing, L.; Li, S.; Yan, W.; Gao, D.; Du, G. Impact-Rubbing Dynamic Behavior of Magnetic-Liquid Double Suspension Bearing under Different Protective Bearing Forms. *Processes* **2021**, *9*, 1105. https://doi.org/10.3390/pr9071105

Academic Editor: Ján Piteľ

Received: 23 March 2021
Accepted: 22 June 2021
Published: 25 June 2021

Publisher's Note: MDPI stays neutral with regard to jurisdictional claims in published maps and institutional affiliations.

Copyright: © 2021 by the authors. Licensee MDPI, Basel, Switzerland. This article is an open access article distributed under the terms and conditions of the Creative Commons Attribution (CC BY) license (https://creativecommons.org/licenses/by/4.0/).

1. Introduction

The magnetic-liquid double suspension bearing (MLDSB) is a new type of suspension bearing, with electromagnetic suspension as the main part and hydrostatic supports as the auxiliary part. With this, the bearing capacity, operation stability, and service life of rotor-bearing systems can be greatly improved. MLDSB is suitable for hydroelectric power, deep-sea exploration, and other fields, especially those that feature a medium speed, heavy load, and frequent starting occasions.

The MLDSB Test Table includes a variable speed motor, coupling, radial bearing, axial bearing, axial loading motor, radial loading motor, step shaft, and frame, as shown in Figure 1 [1].

The radial bearing includes a rotor, magnetic sleeve, supporting cavity, magnetic pole, oil inlet/return hole, shell, and coil, as shown in Figures 2 and 3 [1]. The magnetic pole and magnetic guide sleeve were treated with chromium plating to prevent them from being corroded due to their immersion in oil for a long time [2,3].

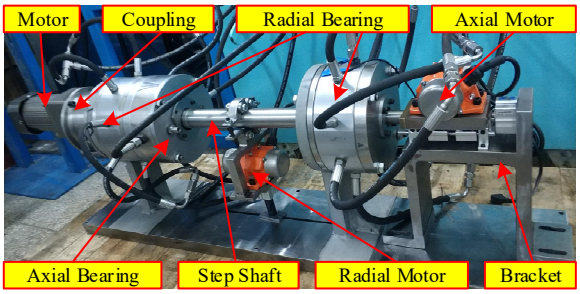


Figure 1. MLDSB Test Table.

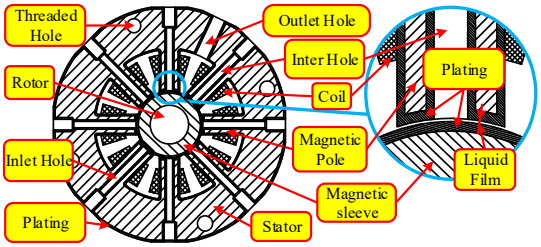


Figure 2. Cutaway view of the Radial Unit.

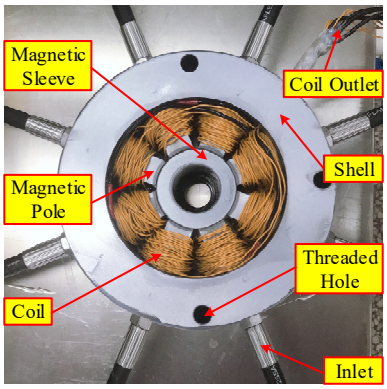


Figure 3. Photo of the Radial Unit.

The regulation principle of MLDSB is shown in Figure 4 [1]. The PD control and constant pressure supply mode are adopted in the electromagnetic system and hydrostatic system, respectively, to realize real-time regulation of the rotor [1].

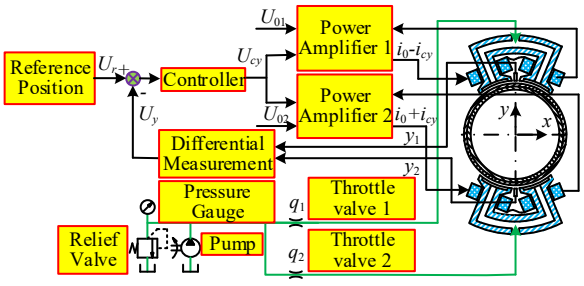


Figure 4. Single DOF control system of MLDSB.

Electromagnetic system failure, which is caused by electromagnetic coil corrosion and power amplifier circuit fault [4,5], will lead to friction and excessive wear between the rotor and magnetic pole, causing the structural strength and reliability of the electromagnetic bearing to be severely reduced. Thus, the fixed ring/deep groove ball bearings and other protective devices are equipped with AMB (Active Magnetic Bearings) to improve the operation stability.

In recent years, many scholars at home and abroad have deeply studied the impact-rubbing dynamics of AMB and achieved many results.

Professor JARROUX [6] studied the rotor drop dynamics numerically and experimentally when AMB unexpectedly stops. The finite unit method and three kinds of TDB models were used to simulate rotor drops in the time domain and measure rotor drop responses, according to the displacement and transmission load.

Professor PATPICK [7] studied the control scheme of AMB when intermittent fault or overload occurs. The results showed that proper forced phase synchronization can destabilize the synchronous forward friction response. The rotor under contact rubbing and slight rotational motion is beneficial to the system and does not interfere with the main electromagnetic bearing control loop.

A robust control strategy to ensure suspension recovery was proposed by Professor PESCH [8]. The specific AMB control laws were found by using model-based optimization synthesis to explain and prevent electromagnetic levitation failure, caused by large deformations, using control contact force saturation.

The dynamic model was established by Professor Zhao [9] to study the dynamic characteristics of rotor drops, and a PID control system for a magnetic bearing was designed with contact possibilities. The control strategy was theoretically demonstrated to be effective in returning a rotor to the contact-free levitation position and avoid further fierce contacts under several circumstances involving external disturbances.

The falling behavior of the spindle structure of a vertical axis magnetic levitation wind turbine was simulated by Professor Wu [10] The movement track of the spindle in the axial direction was compared to visually illustrate the influence of different protective bearing structures on the movement track of the magnetic suspension spindle in the falling process.

The situation of the AMB falling on the self-eliminating clearance protection bearing after failure was studied by Professor Xu [11–14]. Compared with the traditional roller bearing, the self-eliminating clearance protection bearing significantly reduced the vibration of the rotor after falling, and the falling of the high frequency speed was more reliable.

Professor Zdzislaw [15] studied H∞ and H2 control of rigid rotor movement, which is supported in magnetic bearings, and investigated the robust control of magnetic bearings. The paper proposes robust control with a multi-objective controller to achieve good robust stability when the model of a plant is uncertain. Finally, the success of the robust control is verified by numerical simulation results.

Compared with the traditional AMB, the hydrostatic system is used in MLDSB here to replace the protection devices, so that it not only effectively supports the rotor, but can also buffer the friction fault of the rotor. In this way, the wear degree and probability between the rotor and the magnetic pole can be reduced. However, the protection mechanism of the rotor/stator by the static pressure system in this new bearing system is not clear yet, and the difference between the static pressure system and the traditional protection bearing needs to be explored. Therefore, the dynamic equations of the rotor impact-rubbing in three kinds of protection devices (fixed ring/deep groove ball bearing/hydrostatic system) under electromagnetic failure mode are established in this paper, and the axial trajectory, motion law, and dynamic behavior characteristics of the rotor are numerically simulated and analyzed.

2. Rotor Impact-Rubbing Model during Electromagnetic Failure

The time of rotor impact-rubbing is very short, so the assumptions are as follows [16,17]:

(1) There is a local elastic collision between the magnetic pole and the magnetic jacket, and the deformation is elastic deformation;
(2) The winding magnetic flux leakage, edge magnetic flux, eddy current loss, core material saturation, and coupling effect between magnetic poles are ignored;
(3) The tiny gaps between the poles are ignored;
(4) The inertial force and viscous pressure characteristics of the liquid are ignored;
(5) The gravity of the inner ring of deep groove ball bearings is ignored;
(6) The deep groove ball bearing is simplified into a spring damping system with mass.

2.1. Impact-Rubbing Dynamics Model of the "Rotor-Fixed Ring"

The mechanical model of rotor impact-rubbing on the fixed ring protection device in electromagnetic failure mode is shown in Figure 5, and the mathematical equations of the supporting system are shown as follows [18].

$$\begin{cases} F_{Mx,j} + F_x = m\ddot{x} \\ F_{My,j} + F_y - mg = m\ddot{y} \\ J\ddot{\theta} = -F_t r \end{cases} \tag{1}$$

$$\begin{cases} F_{Mx,j} = \frac{\mu_0 SN^2 \cos\varphi}{2} \sum\limits_{j=1}^{2} (-1)^{j+1} \left[\frac{i_0 + (-1)^j \left(k_{px} y + k_{dx} \dot{x} \right)}{h_0 + 2l + (-1)^j x \cos\varphi} \right]^2 \\ F_{My,j} = \frac{\mu_0 SN^2 \cos\varphi}{2} \sum\limits_{j=1}^{2} (-1)^{j+1} \left\{ \frac{i_0 + (-1)^j \left[\frac{-mg(h_0+2l)^2}{2\mu_0 i_0 SN^2 \cos\varphi} + k_{py} y + k_{dy} \dot{y} \right]}{h_0 + 2l + (-1)^j y \cos\varphi} \right\}^2 \end{cases} \tag{1a}$$

$$\begin{cases} F_n = \begin{cases} k_1 \left(\sqrt{x^2 + y^2} - h_1 \right)^{e_1} + c_1 \frac{\dot{x}x + \dot{y}y}{\sqrt{x^2+y^2}} & \sqrt{x^2 + y^2} - h_1 \geq 0 \\ 0 & \sqrt{x^2 + y^2} - h_1 < 0 \end{cases} \\ F_t = f_1 F_n \\ F_x = \frac{-F_n}{\sqrt{x^2+y^2}} (x - f_1 y) \\ F_y = \frac{-F_n}{\sqrt{x^2+y^2}} (f_1 x + y) \end{cases} \tag{1b}$$

where F_{Mx} and F_{My} are the electromagnetic supporting forces in the x and y directions [19]. F_x and F_y are the components of the impact-rubbing force in the x and y directions. m is the rotor mass. g is the gravity acceleration. J is the inertia moment around the centroid of the rotor. θ is the angular displacement. F_n and F_t are the radial and tangential impact-rubbing forces [20]. R is the radius of the rotor. φ is the angle between the magnetic pole and the center line of the rotating shaft. h_0 and h_1 are the initial unilateral clearance between the rotor and magnetic pole and the inner ring of the protection device, respectively. μ_0 is the vacuum permeability. l is the coating thickness. i_0 is the bias current. S is the area of the magnetic poles. N is the number of coil turns. k_{px} and k_{dx} are the scale and differential coefficients in the x direction. k_{py} and k_{dy} are the proportional and differential coefficients in the y direction. e_1, k_1, c_1, and f_1 are the contact coefficient, stiffness, damping, and friction coefficient of the rotor in contact with the inner ring of the protection device, respectively.

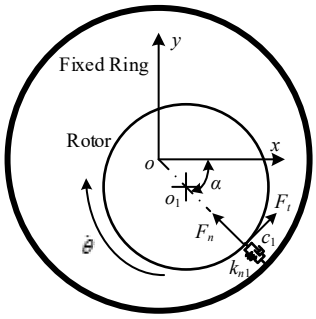


Figure 5. Mechanical model of the "rotor-fixed ring" protection device.

Electromagnetic system failure in the paper includes the failure of solely the upper unit and the failure of the upper and lower units. The mathematical model of the impact-rubbing dynamics is shown in Equation (1), which just requires the following changes:

$$\begin{cases} F_{My,1} = 0 & \text{Upper unit failure} \\ F_{My,1} = F_{My,2} = 0 & \text{Upper/Lower units failure} \end{cases} \tag{2}$$

2.2. Impact-Rubbing Dynamics Model of the "Rotor-Deep Groove Ball Bearing"

The mechanical model of the rotor impact-rubbing on the deep groove ball bearing under electromagnetic failure mode is shown in Figure 6, and the mathematical model of the supporting system is shown as follows [18].

$$\begin{cases} F_{Mx,j} + F_{x1} = m\ddot{x} \\ F_{My,j} + F_{y1} - mg = m\ddot{y} \\ J\ddot{\theta} = -F_{t1}r \\ F_{x2} - F_{x1} = m_b\ddot{x}_b \\ F_{y2} - F_{y1} = m_b\ddot{y}_b \\ J_b\ddot{\theta}_b = (F_{t2} - F_{t1})(h_1 + r) \end{cases} \tag{3}$$

$$\begin{cases} F_{n1} = \begin{cases} k_1\left[\sqrt{(x-x_b)^2 + (y-y_b)^2} - h_1\right]^{e_1} + c_1\frac{(\dot{x}-\dot{x}_b)(x-x_b)+(\dot{y}-\dot{y}_b)(y-y_b)}{\sqrt{(x-x_b)^2+(y-y_b)^2}} & \sqrt{(x-x_b)^2 + (y-y_b)^2} - h_1 \geq 0 \\ 0 & \sqrt{(x-x_b)^2 + (y-y_b)^2} - h_1 < 0 \end{cases} \\ F_{t1} = f_1F_{n1} \\ F_{x1} = \frac{-F_{n1}}{\sqrt{(x-x_b)^2+(y-y_b)^2}}[(x-x_b) - f_1(y-y_b)] \\ F_{y1} = \frac{-F_{n1}}{\sqrt{(x-x_b)^2+(y-y_b)^2}}[f_1(x-x_b) + (y-y_b)] \end{cases} \tag{3a}$$

$$\begin{cases} F_{n2} = k_2\left(\sqrt{{x_b}^2 + {y_b}^2}\right)^{e_2} + c_2\frac{\dot{x}_bx_b+\dot{y}_by_b}{\sqrt{{x_b}^2+{y_b}^2}} \\ F_{t2} = f_2F_{n2} \\ F_{x2} = \frac{F_{n2}}{\sqrt{{x_b}^2+{y_b}^2}}(x_b - f_2y_b) \\ F_{y2} = \frac{F_{n2}}{\sqrt{{x_b}^2+{y_b}^2}}(f_2x_b + y_b) \end{cases} \tag{3b}$$

where F_{x1} and F_{y1} are the components of the impact-rubbing force acting on the rotor in the x and y directions. m_b is the mass of the bearing's inner ring. F_{x2} and F_{y2} are the components of the impact-rubbing force acting on the inner ring of the bearing in the x and y directions. x_b and y_b are the displacements of the bearing's inner ring in the x and y directions. J_b is the moment of inertia of the bearing's inner ring around the centroid. θ_b is the angular displacement of the bearing's inner ring. F_{n1} and F_{t1} are the radial and tangential impact-rubbing forces acting on the rotor. F_{n2} and F_{t2} are the radial and tangential impact-rubbing forces acting on the inner ring of the bearing. e_2, k_2, c_2, and f_2 are the contact coefficient, stiffness, damping, and friction coefficient of the bearing's inner ring in contact with the ball, respectively.



(**a**) Initial equilibrium stage. (**b**) Contact and rubbing stage.

Figure 6. Mechanical model of the protection device for the "rotor-deep groove ball bearing".

The mathematical model of the impact-rubbing dynamics in the deep groove ball bearing is shown in Equation (3), which requires the changes as shown in Equation (2).

2.3. Impact-Rubbing Dynamics Model of the "Rotor-Hydrostatic System"

The mechanical model of the impact-rubbing dynamics on the hydrostatic system under electromagnetic failure mode is shown in Figure 7, and the mathematical model of the supporting system is shown as follows.

$$\begin{cases} F_{Lx,j} + F_{Mx,j} + F_x = m\ddot{x} \\ F_{Ly,j} + F_{My,j} + F_y - mg = m\ddot{y} \\ J\ddot{\theta} = -F_t r \end{cases} \tag{4}$$

$$\begin{cases} F_{Lx,j} = \sum\limits_{j=1}^{2} \left\{ \dfrac{(-1)^j 2p_s A_e \cos\varphi}{1+(\beta-1)\left[1+(-1)^j \frac{x}{h_0}\cos\varphi\right]^3} - 2A_b A_e R_{hj,x} \dot{x}\cos\varphi \right\} \\ F_{Ly,j} = \sum\limits_{j=1}^{2} \left\{ \dfrac{(-1)^j 2p_s A_e \cos\varphi}{1+(\beta-1)\left[1+(-1)^j \frac{y}{h_0}\cos\varphi\right]^3} - 2A_b A_e R_{hj,y} \dot{y}\cos\varphi \right\} \end{cases} \tag{4a}$$

$$\begin{cases} R_{hj,x} = \dfrac{\mu}{\overline{B}\left[h_0+(-1)^j x\cos\varphi\right]^3} \\ R_{hj,y} = \dfrac{\mu}{\overline{B}\left[h_0+(-1)^j y\cos\varphi\right]^3} \end{cases} \quad j = 1,2 \tag{4b}$$

where F_{Lx} and F_{Ly} are the hydrostatic force in the x and y directions [21]. p_s is the oil supply pressure. A_e and A_b are the effective bearing area and extrusion area of the supporting cavity, respectively. R_{hj} is the fluid resistance of the bearing cavity after loading. μ is the oil viscosity. $\overline{B}$ is the flow coefficient [22]. β is the throttling ratio.

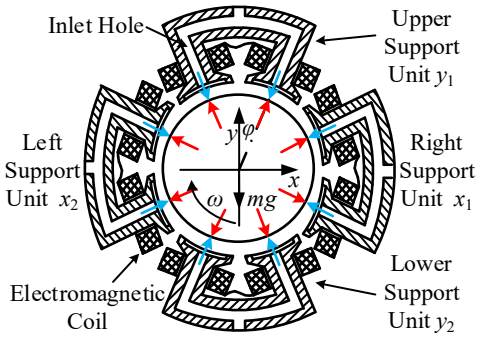


Figure 7. Mechanical model of the protection device for the "rotor- hydrostatic system".

The mathematical model of the impact-rubbing dynamics in the hydrostatic system is shown in Equation (4), which requires the changes as shown in Equation (2).

3. Numerical Simulation of the Rotor Impact-Rubbing Process under Electromagnetic Failure

The initial design parameters of the fixed ring/deep groove ball bearing/hydrostatic system support are shown in Table 1.

Table 1. Initial design parameters of the protection device.

Rotor Mass m**/(kg)**	**Gravitational Acceleration** g**/(m/s^2)**	**Rotor Radius** r**/(m)**	**Rotor Rotational Inertia** J**/(kg·m^2)**
10	10	0.1	0.05
Angle $\varphi/(^\circ)$	Bias current $i_0/(\mathrm{A})$	Coating thickness $l/(\mu\mathrm{m})$	Initial unilateral clearance $h_0/(\mu\mathrm{m})$
22.5	0.5	50	50
Magnetic area $S/(\mathrm{mm}^2)$	Vacuum permeability $\mu_0/(\mathrm{H/m})$	Coil number $N/(\mathrm{dimensionless})$	Stator contact coefficient $e_1/(\mathrm{dimensionless})$
1080	$4\pi \times 10^{-7}$	50	10/9
Stator damping $c_1/(\mathrm{N{\cdot}m/s})$	Stator stiffness $k_1/(\mathrm{N/m^{-10/9}})$	Stator friction coefficient $f_1/(\mathrm{dimensionless})$	Inner ring unilateral clearance $h_1/(\mu\mathrm{m})$
1000	3.5×10^8	0.1	25
Inner ring rotational inertia $J_b/(\mathrm{kg{\cdot}m^2})$	Inner quality $m_b/(\mathrm{kg})$	Inner ring friction coefficient $f_2/(\mathrm{dimensionless})$	Contact coefficient $e_2/(\mathrm{dimensionless})$
1×10^{-4}	0.01	0.007	1.5
Ball bearing stiffness $k_2/(\mathrm{N/m^{-3/2}})$	Ball bearing damping $c_2/(\mathrm{N{\cdot}m/s})$	Oil supply pressure $p_s/(\mathrm{MPa})$	Extrusion area $A_b/(\mathrm{mm}^2)$
4×10^{12}	800	0.05	56
Oil viscosity $\mu/(\mathrm{Pa{\cdot}s})$	Throttling ratio $\beta/(\mathrm{dimensionless})$	Discharge coefficient/(dimensionless)	Effective bearing area $A_e/(\mathrm{mm}^2)$
1.3×10^{-3}	2	0.71	416

3.1. Impact-Rubbing Dynamics Behavior of the Rotor-Fixed Ring Supporting System

1. Impact-rubbing behavior of the rotor under upper unit failure mode

The axis trajectory of the rotor falling on the fixed ring under upper unit failure mode is shown in Figure 8.

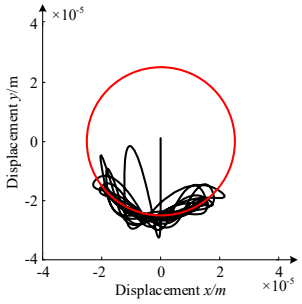
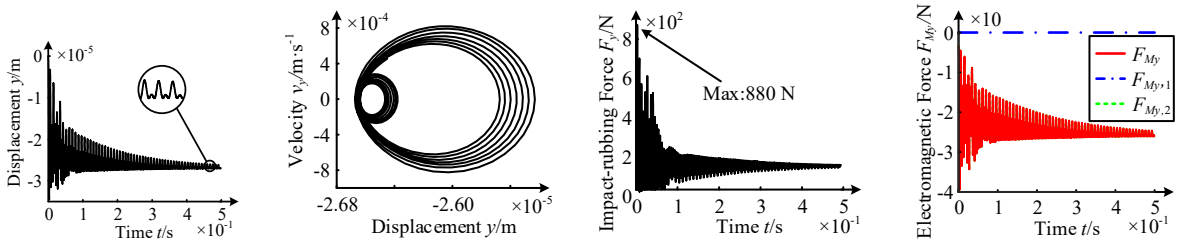


Figure 8. Axis trajectory under upper unit failure mode.

According to Figure 8, the impact-rubbing phenomenon of the rotor can be divided into the bouncing stage and eddy stage, when the upper unit fails. When the rotor falls directly on the fixed ring, it firstly bounces and collides and then vortexes repeatedly forward/backward.

In order to further analyze the bounce-eddy situation of the rotor falling, the rotor displacement, phase trajectory, rubbing force, and electromagnetic force were extracted, as shown in Figure 9.



(**a**) Displacement (**b**) Phase trajectory (**c**) Impact-rubbing force (**d**) Electromagnetic force

Figure 9. Operating law under upper unit failure.

According to Figure 9, the bouncing stage mainly occurs within 0.07 s. The rotor displacement, impact-rubbing force, and residual electromagnetic force shake violently, and their amplitudes gradually decrease. The maximum impact-rubbing force is 880 N.

The eddy stage mainly occurs after 0.07 s. The displacement gradually converges at about −26 μm, which is larger than the unilateral air gap, indicating that the rotor will eventually stagnate at the bottom of the fixed ring. The phase trajectory presents a double-periodic closed circle from the outside to the inside, which indicates the displacement tends to converge. The variation of the impact-rubbing force/electromagnetic force is similar to that of the displacement, respectively, converging at about 125 N and −25 N, and their vector sums are just in balance with the rotor's gravity.

2. Impact-rubbing behavior under upper and lower unit failure

The axis trajectory of the rotor under upper and lower unit failure mode is shown in Figure 10.

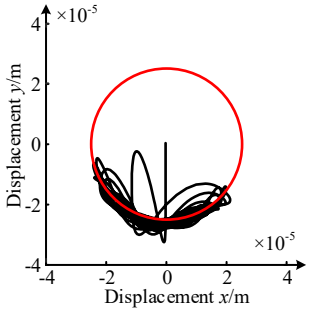
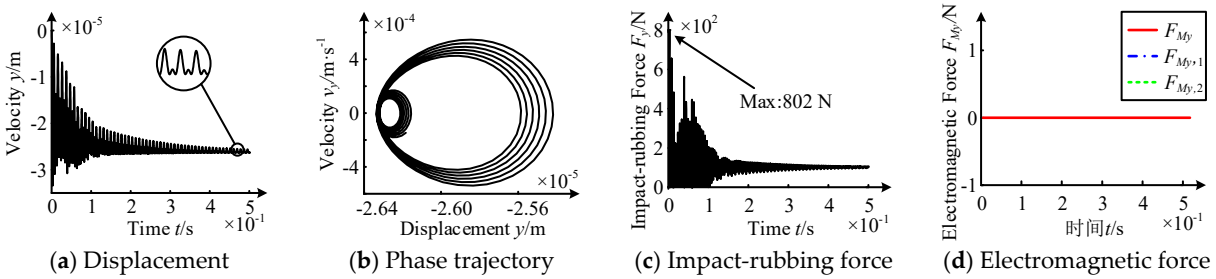


Figure 10. Axis trajectory under upper and lower unit failure.

Similarly, the impact-rubbing phenomenon of the rotor can be divided into the bouncing stage and eddy stage, when the upper unit fails. When the rotor falls directly on the fixed ring, it bounces and collides firstly and then vortexes repeatedly forward/backward.

Similarly, the rotor displacement, phase trajectory, rubbing force, and electromagnetic force were extracted, as shown in Figure 11.



(**a**) Displacement (**b**) Phase trajectory (**c**) Impact-rubbing force (**d**) Electromagnetic force

Figure 11. Operating law of the system under the failure of the upper and lower units.

According to Figure 11, the bouncing stage mainly occurs within 0.1 s. The rotor displacement, impact-rubbing force, and residual electromagnetic force shake violently, and their amplitudes gradually decrease. The maximum impact-rubbing force is 802 N.

The eddy stage mainly occurs after 0.1 s. In this stage, the displacement gradually converges at about −26 μm, which indicates the rotor will eventually stagnate at the bottom of the fixed ring. The phase trajectory presents a double-periodic closed circle from the outside to the inside, which indicates that the displacement tends to converge. There is no residual electromagnetic force, and the variation of the impact-rubbing force is similar to that of the displacement, converging at about 100 N, and the vector value is just in balance with the rotor's gravity.

3.2. Impact-Rubbing Dynamics Behavior of the Rotor-Ball Bearings Supporting System

1. Impact-rubbing behavior law under upper unit failure

In the upper unit failure mode, the axis trajectory of the rotor falling in the deep groove ball bearing is shown in Figure 12.

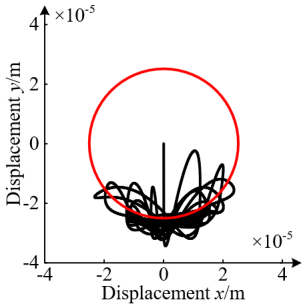


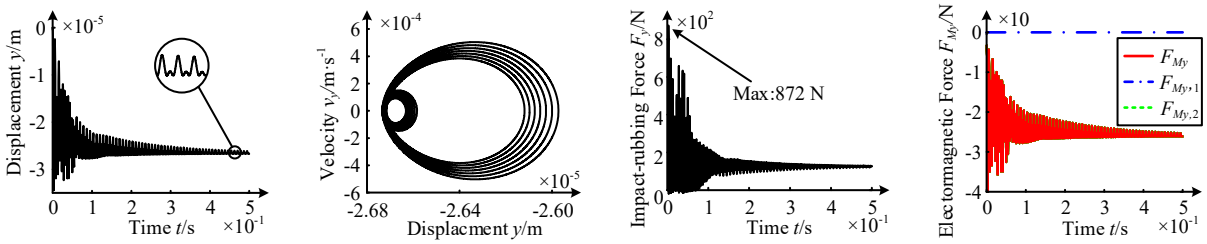
Figure 12. Axial trajectory under upper unit failure.

Similarly, the impact-rubbing phenomenon of the rotor can be divided into the bouncing stage and eddy stage, when the upper unit fails. When the rotor falls directly on the inner ring of the ball bearing, it bounces and collides firstly and then vortexes repeatedly forward/backward.

Similarly, the rotor displacement, phase trajectory, rubbing force, and electromagnetic force were extracted, as shown in Figure 13.

According to Figure 13, the bouncing stage mainly occurs within 0.06 s. The rotor displacement, impact-rubbing force, and residual electromagnetic force shake violently, and their amplitudes gradually decrease. The maximum impact-rubbing force is 872 N.

The eddy phase mainly occurs after 0.06 s, and the displacement gradually converges at about −26 μm, which is larger than the unilateral air gap, indicating that the rotor will eventually stagnate at the bottom of the inner ring. The phase trajectory presents a double-periodic closed circle from the outside to the inside, which indicates the displacement tends to converge. The variation of the impact-rubbing force/electromagnetic force is similar to that of the displacement, respectively converging at about 126 N and −26 N, and their vector sums are just in balance with the rotor's gravity.



(**a**) Displacement (**b**) Phase trajectory (**c**) Impact-rubbing force (**d**) Electromagnetic force

Figure 13. Operating law under upper unit failure.

2. Impact-rubbing behavior law under upper and lower unit failure

In upper and lower unit failure mode, the axis trajectory of the rotor falling is shown in Figure 14.

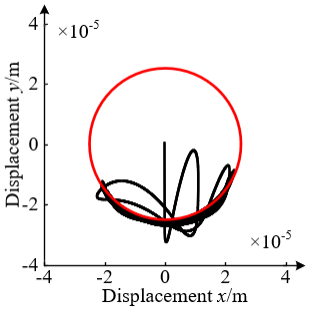
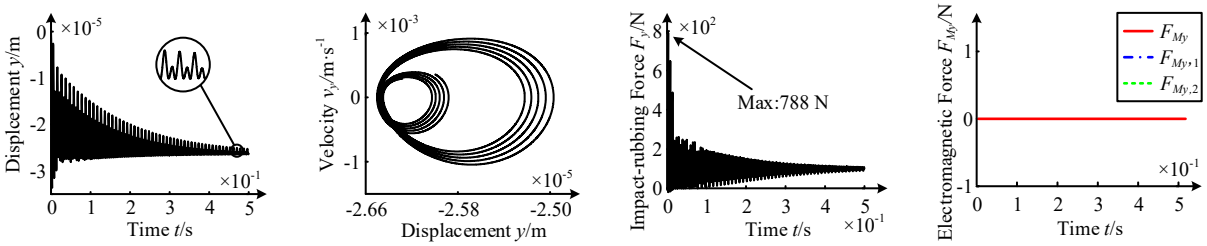


Figure 14. Axial trajectory under upper and lower unit failure.

Similarly, the impact-rubbing phenomenon of the rotor can be divided into the bouncing stage and eddy stage, when the upper unit fails. When the rotor falls directly on the inner ring of the ball bearing, it bounces and collides firstly and then vortexes repeatedly forward/backward.

Similarly, the rotor displacement, phase trajectory, rubbing force, and electromagnetic force were extracted, as shown in Figure 15.



(**a**) Displacement (**b**) Phase trajectory (**c**) Impact-rubbing force (**d**) Electromagnetic force

Figure 15. Operating law under upper and lower unit failure.

According to Figure 15, the bouncing stage mainly occurs within 0.02 s. Both the rotor displacement and impact-rubbing force shake violently. The amplitude decreases gradually, and the maximum impact-rubbing force value is 788 N.

The vortex stage mainly occurs after 0.02 s. The displacement gradually converges at about −26 μm in this stage, indicating that the rotor will eventually stagnate at the bottom of the inner ring. The phase trajectory presents a double-periodic closed circle from the outside to the inside, which indicates that the displacement tends to converge. There is no residual electromagnetic force. The variation of the impact-rubbing force is similar to that

of the displacement, respectively converging at about 100 N, and the vector value is just in balance with the weight of the rotor.

3.3. Impact-Rubbing Dynamics Behavior of the Rotor-Hydrostatic System

1. Impact-rubbing behavior law under upper unit failure

In upper unit failure mode, the axis trajectory of the rotor falling in the hydrostatic system is shown in Figure 16.

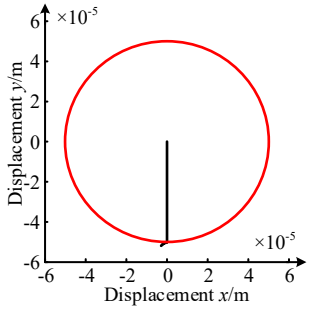
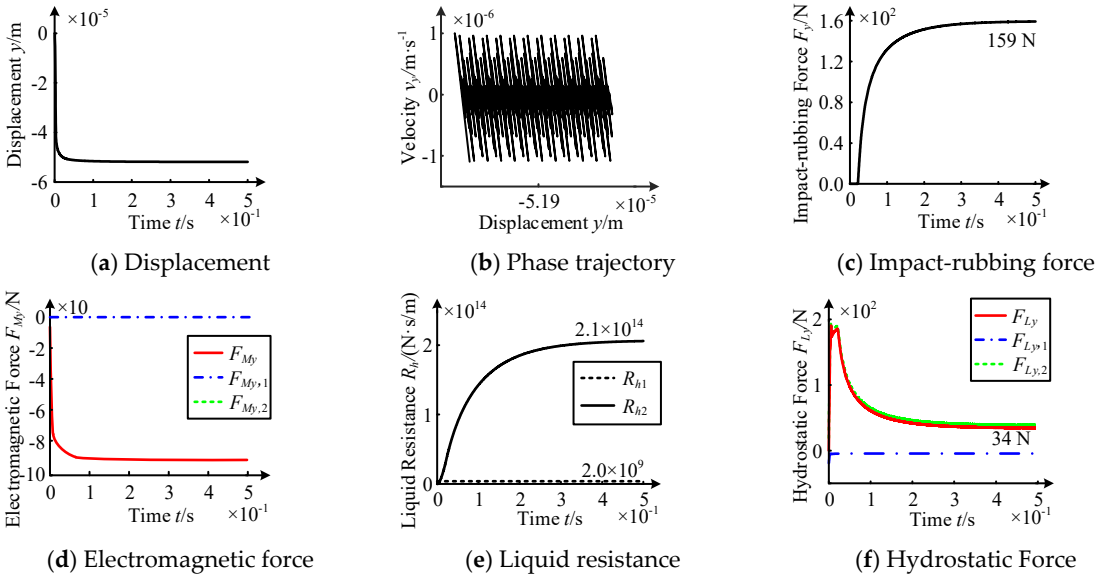


Figure 16. Axial trajectory under upper unit failure.

According to Figure 16, when the upper unit fails, the rotor directly falls to the magnetic pole with the contact and friction of a small tremor.

In order to analyze the impact-rubbing situation in the rotor-hydrostatic system, the rotor displacement, phase trajectory, rubbing force, electromagnetic force, hydraulic resistance, and hydrostatic force were extracted, as shown in Figure 17.



(**a**) Displacement (**b**) Phase trajectory (**c**) Impact-rubbing force

(**d**) Electromagnetic force (**e**) Liquid resistance (**f**) Hydrostatic Force

Figure 17. Operating law under upper unit failure.

According to Figure 17, the drop stage mainly occurs within 0.02 s. The rotor displacement decreases rapidly, which means the rotor has a high speed, resulting in a rapid rise in the hydrostatic supporting force F_{Ly}. The fluid resistance R_{h1} of the upper supporting unit almost does not change, but the fluid resistance R_{h2} of the lower supporting unit increases due to the dynamic extrusion effect. The residual electromagnetic force F_{My} decreases rapidly.

The impact-rubbing contact stage mainly occurs after 0.02 s, and the rotor reaches a new equilibrium state: the phase trajectory shows the rotor displacement can achieve

about −51.9 μm and the rotor vibrates periodically at this position at a low speed. As the contact depth between the rotor and stator increases gradually, the impact-rubbing force F_n increases to about 159 N, which can balance the rotor weight with the residual electromagnetic force F_{My} of −93 N and the hydrostatic force F_{Ly} of 34 N. The liquid resistance of the upper supporting unit and the lower supporting unit R_{h1} and R_{h2} respectively stabilize at 2.0 × 10^9 N·s/m and 2.1 × 10^{14} N·s/m.

2. Impact-rubbing behavior law under upper and lower unit failure.

In upper and lower unit failure mode, the axis trajectory of the rotor falling in the hydrostatic system is shown in Figure 18.

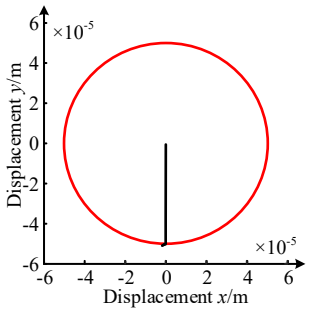
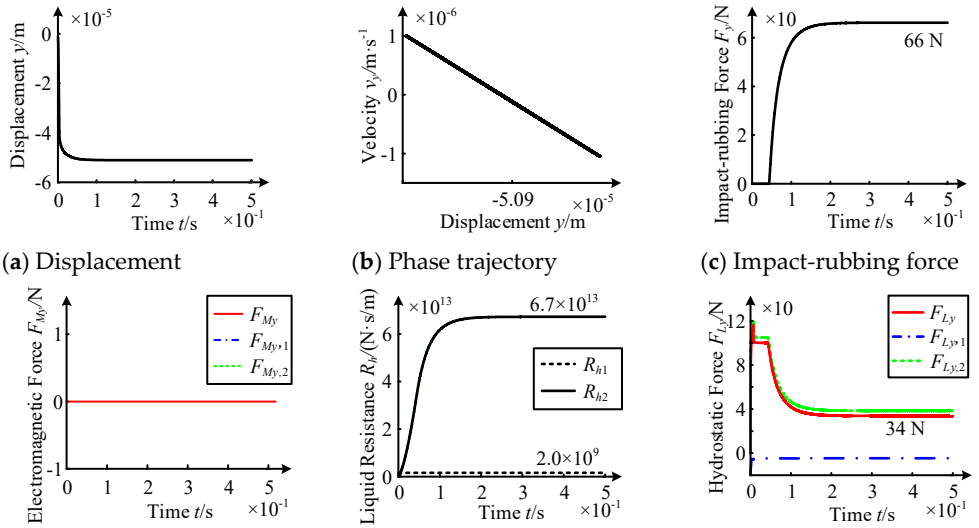


Figure 18. Axial trajectory under upper and lower unit failure.

According to Figure 18, when both the upper and lower units fail, the rotor directly falls to the magnetic pole and collides with a little tremor.

Similarly, the rotor displacement, phase trajectory, impact-rubbing force, electromagnetic force, hydraulic resistance, and hydrostatic force are extracted, as shown in Figure 19.



(**a**) Displacement (**b**) Phase trajectory (**c**) Impact-rubbing force

(**d**) Electromagnetic force (**e**) Liquid resistance (**f**) Hydrostatic Force

Figure 19. Operating law under upper and lower unit failure.

According to Figure 19, the drop stage mainly occurs within 0.04 s. In this stage, the rotor displacement decreases rapidly, which indicates the rotor has a high speed, resulting in a rapid rise in the hydrostatic supporting force F_{Ly}. The fluid resistance R_{h2} of the upper supporting unit shows little change, but the fluid resistance R_{h2} of the lower supporting unit increases rapidly due to the dynamic extrusion effect. The resultant electromagnetic force F_{My} is 0.

The collision stage mainly occurs after 0.04 s, and the rotor reaches a new equilibrium state. The phase trajectory shows the rotor displacement can achieve about −51.9 μm and the rotor vibrates periodically at this position at a low speed. With the increase of the contact depth between the rotor and the stator, the impact-rubbing force F_n increases to about 66 N, which can balance the rotor weight with the hydrostatic force F_{Ly} of 34 N. The liquid resistance of the upper supporting unit and the lower supporting unit R_{h1} and R_{h2} respectively stabilize at 2.0×10^9 N·s/m and 6.7×10^{13} N·s/m.

3.4. Comparison of the Three Protection Devices in Impact-RUBBING Behavior

1. Analysis of the impact-rubbing behavior under upper unit failure.

According to Figures 8, 12 and 16, it can be seen that under upper unit failure mode, the axis trajectories of the rotor falling in the fixed ring/deep groove ball bearings are basically the same. They both remain in the bouncing stage for a long time, followed by the forward/backward eddy stage, with a low value. Due to the dynamic extrusion effect of oil, only small tremors occur near the falling position of the rotor when it falls in the hydrostatic system, and there is no complex bouncing and eddy phenomena.

According to Figures 9, 13 and 17, it can be seen that the rotor displacement falling in the hydrostatic system is relatively stable in comparison with the fixed ring and deep groove ball bearing protection devices. The phase trajectory is no longer a double-periodic closed circle from the outside to the inside, but a periodic superposition with the same frequency. Compared with the fixed ring and deep groove ball bearings, the maximum impact force respectively decreases by 81.9% and 81.8% in the hydrostatic system. The variation of the residual electromagnetic force is gentler.

2. Analysis of the impact-rubbing behavior under upper and lower units.

According to Figures 10, 14 and 18, it can be seen that under upper and lower unit failure mode, the axis trajectory of the rotor falling in the fixed ring firstly remains for a long time in the bouncing stage and then presents a low value for the forward/backward vortex phenomenon. A short bouncing phenomenon occurs in the case of falling in the deep groove ball bearing, and then presents a longer lasting time for the forward/backward vortex phenomenon. Due to the dynamic extrusion effect, only the small tremor occurs near the drop position in the case of falling in the hydrostatic system, and there is no complex bouncing and eddy phenomena.

According to Figures 11, 15 and 19, compared with the fixed ring and deep groove ball bearing protection devices, the displacement of the rotor falling in the hydrostatic system changes more stably, and only a slight tremor occurs under upper and lower unit failure mode. The phase trajectories show the form of reciprocating motion with the same frequency. The maximum impact force is reduced by 91.8% and 91.6%, and the degree of impact of the bounce and eddy is greatly reduced.

3. Analysis of results.

In summary, the influence of the three protection devices on rotor impact-rubbing under electromagnetic failure mode is shown in Tables 2 and 3.

Table 2. Influence of upper unit failure on impact-rubbing.

Protective Devices	Bounce Time	Eddy	Max. Impact-Rubbing Force	Impact-Rubbing Parts
Fixed ring	<0.07 s	yes	880 N	rotor and fixed ring
Ball bearing	<0.06 s	yes	872 N	rotor and inner ring
Hydrostatic system	none	none	159 N	rotor and pole

Table 3. Influence of upper and lower unit failure on impact-rubbing.

Protective Devices	Bounce Time	Eddy	Max. Impact-Rubbing Force	Impact-Rubbing Parts
Fixed ring	<0.1 s	yes	802 N	rotor and fixed ring
Ball bearing	<0.02 s	yes	788 N	rotor and inner ring
Hydrostatic system	none	none	66 N	rotor and pole

4. Conclusions

1. The influences of the protection devices on the bouncing time, impact-rubbing force, and impact-rubbing degree are found to be as follows: the hydrostatic system shows the best results, followed by the deep groove ball bearing and then the fixed ring.
2. Compared with the fixed ring and deep groove ball bearing, the positions of the rotor impact-rubbing in the hydrostatic system are the rotor and magnetic pole, and the maximum impact-rubbing force is lower without bounce and eddy phenomena.
3. Compared with the bounce time and the maximum impact-rubbing force of the rotor in the three protective devices, it can be seen that there is no bounce phenomenon of the rotor in the hydrostatic system and the maximum impact-rubbing force is greatly reduced, so the protective bear is not required to be installed in the MLDSB.

Author Contributions: Conceptualization, J.Z.; Data curation, J.Z.; Methodology, J.Z.; Project administration, J.Z.; Resources, J.Z. and W.Y.; Software, L.X.; Supervision, D.G. and G.D.; Writing—original draft, L.X.; Writing—review and editing, L.X. and S.L. All authors have read and agreed to the published version of the manuscript.

Funding: This work was supported by the National Nature Science Foundation of China (no. 52075468); General project of Natural Science Foundation of Hebei Province (E2020203052); Youth Fund Project of scientific research project of Hebei University (QN202013); Open Project Funding of Jiangsu Provincial Key Laboratory of Advanced Manufacture and Process for Marine Mechanical Equipment and Open Project Funding of Fluid Power Transmission Control Laboratory of Yanshan University.

Data Availability Statement: Not applicable.

Conflicts of Interest: The authors declare no conflict of interest.

References

1. Zhao, J.H.; Yan, W.D.; Wang, Z.Q.; Gao, D.; Du, G. Study on Clearance-Rubbing Dynamic Behavior of 2-DOF Supporting System of Magnetic-Liquid Double Suspension Bearing. *Processes* **2020**, *8*, 973. [CrossRef]
2. Xiong, W.L.; Hu, C.; Lang, L.; Zheng L, G. Study on the Influence of Controllable Throttle Parameters on the Characteristics of Hydrostatic Bearing. *J. Mech. Eng.* **2017**, *22*, 3354–3359.
3. Zhao, J.H.; Zhang, G.J.; Cao, J.B.; Gao, D.R.; Du, G.J. Decouping Control of Single DOF Supporting System of Magnetic-Liquid Double Suspension Bearing. *Mach. Tool Hydraul.* **2020**, *48*, 1–8.
4. Zu, L.; Wang, H. Design and Research of Rotor Drop Protection System Test Bench. *At. Energy Sci. Technol.* **2015**, *49*, 340–386.
5. Wang, X.H.; Yang, F.F.; Zhao, Q. Dynamics Analysis of Aircraft Engine Rotor Drop after Electromagnetic Bearing Failure. *Gas Turbine Test. Res.* **2019**, *32*, 1–7.
6. Jarroux, C.; Dufour, R.; Mahfoud, J.; Defoy, B.; Alban, T.; Delgado, A. Touchdown Bearing Models for Rotor-AMB Systems. *J. Sound Vib.* **2018**, *440*, 51–69. [CrossRef]
7. Patrick, K.; Matthew, C. Dynamic Conditions to Destabilize Persistent Rotor/Touchdown Bearing Contact in AMB Systems. *Mech. Eng. J.* **2017**, *4*, 17-00005.
8. Pesch, A.H.; Sawicki, J.T.; Maslen, E.H. Active Magnetic Bearing Online Levitation Recovery through μ-Synthesis Robust Control. *Actuators* **2017**, *6*, 2. [CrossRef]
9. Zhao, J.L.; Gong, H.L.; Yang, G.J.; Shi, C.G. Research on Drop Recovery Control Strategy of Electromagnetic Bearing Horizontal Rotor. *Fan Technol.* **2020**, *62*, 38–45.
10. Wu, G.Q.; Lu, B.; He, D.W.; Song, C.G. Influence of Protective Bearing Structure on the Spindle Dropping Trajectory of Vertical Axis Maglev Wind Turbine. *Mech. Des. Res.* **2018**, *34*, 108–110.
11. Wei, P.; Wang, Y.F.; Yang, Y.; Yan, J.L. Research on the Impact Force of High Speed Suspending Rotor Dropping on the Protective Bearing. *Vib. Shock.* **2018**, *37*, 251–258.

12. Yu, C.T.; Xu, L.X.; Jin, C.W. Kinematics Analysis of Protective Clearance Mechanism for Automatic Elimination of Active Magnetic Bearing System. *J. Aviat.* **2015**, *36*, 2485–2496.
13. Zhu, Y.L.; Jin, C.W. Analysis of Maximum Impact Force and Thermal Characteristics of Double Layer Protective Bearings under High Speed and Heavy Duty. *China Mech. Eng.* **2016**, *27*, 25–31. [CrossRef]
14. Zhu, Y.L.; Jin, C.W.; Lian, C.Y.; Zheng, Z.Q. Dynamic Analysis of Vertical Rotor Fall into Deep Groove Ball Protective Bearing. *Mech. Des. Res.* **2017**, *33*, 72–77.
15. Gosiewski, Z.; Mystowski, A. The Robust Control of Magnetic Bearings for Rotating Machinery. *Solid State Phenom.* **2006**, *113*, 125–130. [CrossRef]
16. Ebrahimi, R.; Ghayour, M.; Khanlo, H.M. Nonlinear Dynamic Analysis and Experimental Verification of a Magnetically Supported Flexible Rotor System with Auxiliary Bearings. *Mech. Mach. Theory* **2018**, *121*, 545–562. [CrossRef]
17. Zhao, J.; Chen, H.T.; Wang, Q.; Zhang, B.; Gao, D.R. Stability Analysis of Single DOF Support System of Magnetic-Liquid Double Suspension Bearing. *Hydromechatron. Eng.* **2019**, *47*, 1–7.
18. Jiang, L. Research on Dynamics of Rotor Drop on Auxiliary Bearing. Ph.D. Thesis, Nanjing University of Aeronautics and Astronautics, Nanjing, China, 2011.
19. Weiss, G.; Staffans, O. Maxwell's Equations as a Scattering Passive Linear System. *SIAM J. Control. Optim.* **2013**, *51*, 3722–3756. [CrossRef]
20. Liu, T.; Sun, X.; Wu, J. Study on Extraction of Impact Vibration between Sliding Bearing and Rotor under Different Friction Condition. *Lubr. Seal.* **2018**, *43*, 67–71.
21. Verma, S.; Dewan, A. Partially-Averaged Navier-Stokes (PANS) Approach for Study of Fluid Flow and Heat Transfer Characteristics in Czochralski Melt. *J. Cryst. Growth* **2018**, *481*, 56–64. [CrossRef]
22. Zhao, J.H.; Liang, Y.N.; Gao, D.R. Oil Pocket's Bearing Capacity Analysis of Liquid Hydrostatic Worktable in Gantry Moving Milling Center. *Chin. J. Mech. Eng.* **2014**, *27*, 1008–1017. [CrossRef]